Wave manipulation using a bistable chain with reversible impurities

Hiromi Yasuda [1] Efstathios G. Charalampidis [2] Prashant K. Purohit,[1] Panayotis G. Kevrekidis,[3] and Jordan R. Raney [1,*]

[1]*Department of Mechanical Engineering and Applied Mechanics, University of Pennsylvania, Philadelphia, Pennsylvania 19104, USA*
[2]*Mathematics Department, California Polytechnic State University, San Luis Obispo, California 93407-0403, USA*
[3]*Department of Mathematics and Statistics, University of Massachusetts, Amherst, Massachusetts 01003-4515, USA*

We systematically study linear and nonlinear wave propagation in a chain composed of piecewise-linear bistable springs. Such bistable systems are ideal test beds for supporting nonlinear wave dynamical features including transition and (supersonic) solitary waves. We show that bistable chains can support the propagation of subsonic wave packets which in turn can be trapped by a low-energy phase to induce energy localization. The spatial distribution of these energy foci strongly affects the propagation of linear waves, typically causing scattering, but, in special cases, leading to a reflectionless mode analogous to the Ramsauer-Townsend effect. Furthermore, we show that the propagation of nonlinear waves can spontaneously generate or remove additional foci, which act as effective "impurities." This behavior serves as a new mechanism for reversibly programming the dynamic response of bistable chains.

I. INTRODUCTION

Multistable mechanical metamaterials have attracted increasing attention from various research communities in physics, engineering, and materials science, both because of their unique static and dynamic behavior [1–3]. Indeed, multistability has been leveraged to achieve controlled state changes in engineering applications such as reconfigurable robots [4,5], deployable space structures [6], medical devices [7], and many others.

Even simple discrete systems composed of bistable elements (i.e., bistable lattices) are capable of rich and varied nonlinear dynamics. For example, by tailoring the energy landscape of a bistable element, a bistable lattice can allow the propagation of transition fronts [8–12] where the propagating directions and speed can be manipulated. In addition, recent studies have shown that a bistable chain can support the propagation of solitary waves [13–15].

Here, we study the *in situ* manipulation of the dynamic response of a bistable chain in the broader context of linear and nonlinear wave dynamics. In particular, we showcase a mechanism for controllably inserting reversible effective "impurities" in a bistable chain, arising from the trapping of propagating wave packets. We numerically investigate the amplitude-dependent behavior of a bistable chain that can support not only supersonic solitary waves but, depending on the impact speed, also subsonically propagating wave packets. We find that the propagation of the latter is brought to a halt in the bulk of the chain, leading to the formation of effective impurities (albeit within a homogeneous medium) that may play a central role in subsequent dynamics. More specifically, we demonstrate that the presence of such energy foci affects

the scattering of linear waves. Interestingly, if two such effective impurities are placed next to each other and the system is driven at a specific frequency that leads to the propagation of a linear wave of a particular wave number, complete transmission without reflection can occur in a bistable lattice [16]. This is reminiscent of the half-wavelength resonance [17], widely known in quantum mechanics as the Ramsauer-Townsend (RT) effect [18]. Its simplest instance involves perfect transmission at select energies in one-dimensional (1D) scattering from a square well. Multiple impurities can be created via collisions of a propagating wave packet with an impurity. Note that, hereafter, we will use the term impurity in this loose sense, implying the presence of a standing wave, even though no spatial inhomogeneity is present in the lattice.

Our presentation is organized as follows: Section II discusses the model setup, explains the dynamic response of a 1D bistable chain under impact excitation, and identifies the formation of impurities due to the trapping of a subsonic wave packet. In Sec. III, we investigate the scattering behavior between harmonic waves and single impurities. Section IV explores scattering for the case with multiple impurities. Finally, Sec. V summarizes our findings and presents directions for future studies.

II. BISTABLE CHAINS

We begin our discussion by examining the dynamic response of a 1D lattice under an elastic impact excitation caused by a striker [see Fig. 1(a)]. We define u_n as the relative displacement of the nth particle measured from its equilibrium point. We define the strain of the nth particle as $r_n := u_n - u_{n+1}$. Motivated by the reconfigurability of the bistable lattice we consider the trilinear spring element [see Fig. 1(b)]

*raney@seas.upenn.edu
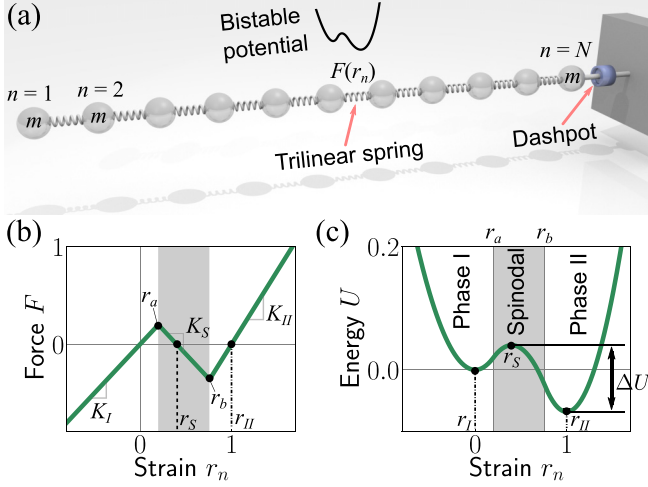
FIG. 1. (a) Schematic illustration of the system composed of bistable springs. The impact is applied to the leftmost unit ($n = 1$) by setting an initial velocity. The rightmost mass ($n = N$) is connected to a dashpot. (b) The relationship between force and strain of a bistable spring is expressed by a trilinear function [cf. Eq. (1)]. The stiffness parameters are $(K_I, K_S, K_{II}) = (1, -1, 1.5)$ and the strain parameters are $(r_S, r_{II}) = (0.4, 1)$. (c) The bistable energy landscape obtained from the trilinear force-strain relationship of panel (b).

defined by the function

$$F(r) = \begin{cases} K_I r & r \leqslant r_a \\ K_S(r - r_S) & r_a \leqslant r \leqslant r_b \\ K_{II}(r - r_{II}) & r_b \leqslant r, \end{cases} \quad (1)$$

where K_I, K_S, and K_{II} are the stiffness parameters. Therefore, Eq. (1) is a double-well potential as shown in Fig. 1(c). In this study, we use the following set of numerical values for the parameters: $(K_I, K_S, K_{II}) = (1, -1, 1.5)$, and $(r_S, r_{II}) = (0.4, 1)$. By using these values, we can determine the other strain parameters: $r_a = K_S r_S/(K_S - K_I)$ and $r_b = (K_S r_S - K_{II} r_{II})/(K_S - K_{II})$. Here, we define the "Phase I" and "Phase II" regimes corresponding to the stable states around $r_I =$

0 and $r_{II} = 1$, respectively [see also Fig. 1(c)]. These two regimes are connected by the spinodal region corresponding to the negative stiffness range [see the shaded gray area in Figs. 1(b) and 1(c)].

Based on this trilinear spring element, the dynamic response of our bistable chain is analyzed by using the following equation of motion:

$$m\ddot{u}_n = F(u_{n-1} - u_n) - F(u_n - u_{n+1}), \quad (2)$$

where m is the mass of the particle whose value is fixed to $m = 1$, and $n = 1, \ldots, N$, with N being the number of particles in the chain. It should be noted that the bistable chain has two sound speeds: $c_I = \sqrt{K_I/m} = 1$ and $c_{II} = \sqrt{K_{II}/m} = \sqrt{1.5}$ corresponding to Phase I and Phase II, respectively.

A. Amplitude-dependent behavior

We analyze strain profiles of propagating waves in a chain consisting of $N = 400$ particles under impact. We numerically simulate the effect of impact by setting the velocity of the first particle to a nonzero value; that is, we set $v_1(t = 0) \neq 0$. All other initial conditions are set to zero [i.e., positions $u_n(t = 0)$ and velocities $v_n(t = 0)$]. Then, we advance Eq. (2) forward in time by using a standard fourth-order Runge-Kutta method. To minimize the effect of reflected waves at the other end of the chain ($n = 400$), the last particle is connected to a dashpot in which the damping force is linearly proportional to the velocity of the last particle ($F_v = \nu v_N$ with $\nu = 1$). The right end of the chain is attached to a rigid wall, i.e., $u_{401}(t) \equiv v_{401}(t) = 0 \; \forall \; t \geqslant 0$. Note that the total energy, which is composed of elastic energy and kinetic energy of each unit, before waves reach the last particle ($n = 400$) which is connected to the dashpot is conserved within $10^{-7}\%$ in each simulation.

We now discuss Fig. 2, which shows the space-time contour plots of the strain variable for four different values of impact velocities: $v_1(t = 0) = 0.1, 0.552, 2$, and 15. In particular, if $v_1(t = 0) = 0.1$, we only observe small-amplitude wave propagation and the chain configuration remains in Phase I [see Fig. 2(a)]. If we increase the impact velocity
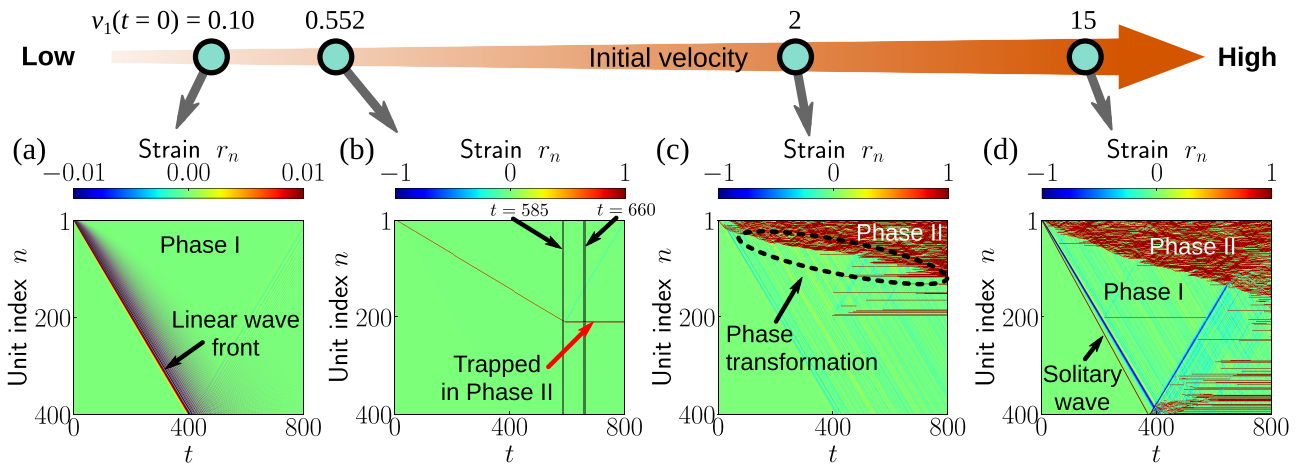
FIG. 2. Amplitude-dependent behavior for a bistable chain composed of strain-hardening springs ($K_{II}/K_I = 1.5$). All unit cells are initially in Phase I. We apply an impact velocity to the first unit cell ($n = 1$) by setting $v_1(t = 0) \neq 0$. We consider four different values of the impact velocities: (a) $v_1(t = 0) = 0.1$, (b) 0.552, (c) 2, and (d) 15. The color indicates the strain r_n as a function of the unit index n and time t.
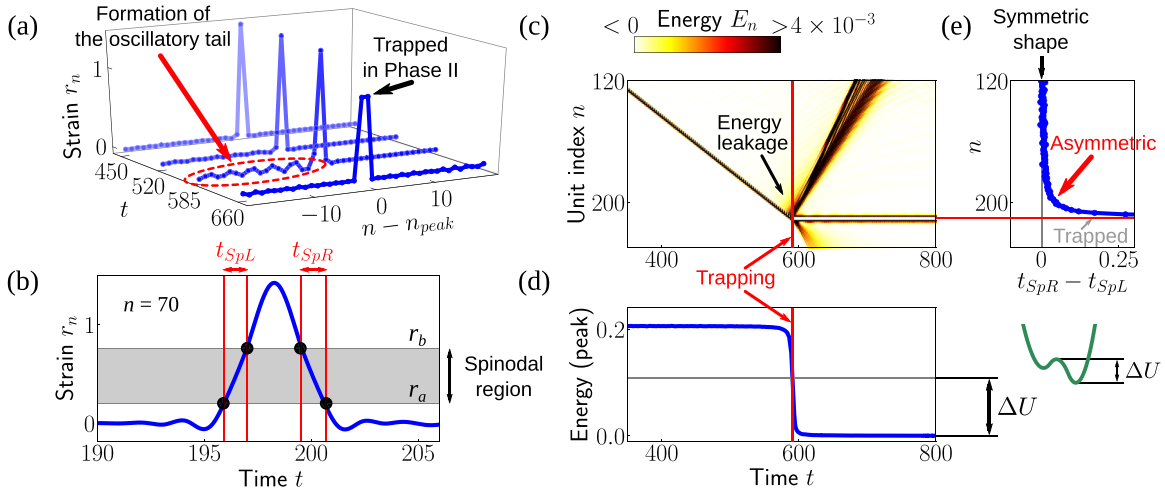
FIG. 3. Trapping behavior. (a) The spatial distribution of the subsonic wave packet generated by the impact velocity $v_1(t = 0) = 0.552$ is shown at different instants of time t. The waveforms for $t = 585$ and 660 correspond to the black vertical lines in Fig. 2(b), respectively. Each strain profile is shifted in the space domain so that the peak of the strain profile is located at $n = 0$ to ease visualization. (b) The strain change of $n = 70$ is shown as a function of time t. The shaded gray area indicates the spinodal regime [see also Fig. 1(c)]. To quantify the wave shape, we measure time widths in which the strain is in the spinodal region, t_{SpL} and t_{SpR}, bounded by the red vertical lines. (c) Surface plot of the energy $E_n(t) = \frac{1}{2} m \dot{u}_n^2(t) + U_n(t)$ where U_n is the bistable potential-energy function of Fig. 1(c). Note that the colormap is adjusted for clarity of illustration of the energy leakage so that energies greater than 4×10^{-3} all appear with a dark color. (d) The peak energy of the propagating wave packet is shown as a function of t. ΔU is the energy barrier measured from the energy minimum in Phase II [see Fig. 1(c)]. The red vertical line indicates the trapping point at which the peak energy becomes lower than that of the energy barrier ΔU. (e) We calculate the time difference $t_{SpR} - t_{SpL}$, which indicates the symmetric (if $t_{SpR} - t_{SpL} = 0$) or asymmetric waveform (otherwise).

to $v_1(t = 0) = 0.552$, we observe the formation of a propagating localized wave packet with amplitude (in the strain variable) greater than $r_S = 0.4$ [see Fig. 2(b)]. This finding indicates that spring elements undergo a transition from Phase I to Phase II and then back to Phase I as the wave packet propagates in the chain. It is noteworthy that the speed of this excitation ($V_{tw} = 0.358$) is slower than that of the small-amplitude wavefront [see Figs. 2(a) and 2(b)]. That is, this is a subsonic propagating wave packet. Interestingly, this structure is brought to a halt before it reaches the end of the chain, and two adjacent spatial nodes are trapped in Phase II [see the red arrow in Fig. 2(b)], forming the effective impurity discussed above. Note that we observe this trapping behavior for the hardening case (i.e., $K_{II}/K_I = 1.5$), however, the chain with softening springs (e.g., $K_{II}/K_I = 0.5$) does not show the formation of impurities or of propagating excitations (see Appendix A for details). Also, in the hardening case ($K_{II}/K_I = 1.5$) with the same input impact, we only observe the formation of the effective impurity composed of two adjacent nodes. Although the propagation of supersonic solitary waves in a nonintegrable Fermi-Pasta-Ulam chain [19,20], specifically a bistable chain [13–15], has been reported previously, the formation of impurities arising from the spontaneous trapping behavior we observe in the present work has been unexplored, to the best of our knowledge.

If $v_1(t = 0)$ is further increased to 2, the chain exhibits a phase transformation of multiple units which propagate from the left end of the chain to the other end, as shown in Fig. 2(c). Finally, when we apply an extremely-large-amplitude input to the system [$v_1(t = 0) = 15$], we find both propagation of a solitary wave ($V_{tw} = 1.076$) and a phase transformation

front [see Fig. 2(d)]. This solitary wave propagates faster than the (linear) sonic wave (i.e., it is a supersonic solitary wave). Appendix B provides an analytical characterization of this supersonic solitary wave based on the Padé approximation [13,14]. In this case, the resonance mechanism with linear waves is absent and hence there is no channel of energy dispersion available to the wave that accordingly propagates without distortion throughout the lattice (once it is "distilled").

Therefore, we find that this bistable chain can support coherent structures of both subsonic and supersonic nature, depending on the magnitude of the impact velocity. We discuss the trapping of subsonically propagating wave packets in the next section.

B. Trapping behavior

To understand this trapping behavior thoroughly, we examine the time evolution of the subsonic propagating wave packet by extracting the strain waveforms at different time frames, especially right before the trapping occurs. In particular, Fig. 3(a) shows the strain profiles for four different time frames: $t = 450$, 520, 585, and 660, [the shapes at $t = 585$ and 660 correspond to the black vertical lines in Fig. 2(b)]. Note that the wave profiles are shifted in the spatial domain so that the peak of the wave is located at the center of the domain to ease visualization. The subsonic localized pattern propagates without any noticeable distortions initially [see also Fig. 3(b) for the strain change of $n = 70$ as a function of time t], although, as time passes, the profile features an oscillatory tail, as can be discerned at $t = 585$ (just before the wave stops) and which is denoted by the red dashed ellipse

in Fig. 3(a). This tail pattern stems from the resonance of the frequency associated with the solitary wave motion with the frequencies of linear modes associated with the (zero) background.

Indeed, as the wave propagates, the profile loses energy in the form of emitted radiation. This is investigated in Figs. 3(c) and 3(d), which depict the spatiotemporal evolution of the total energy of the system and the peak of the energy as a function of time, respectively. As the wave propagates within the chain, the peak energy remains nearly constant, until an abrupt drop in the form of radiation immediately prior to trapping (i.e., when the total energy becomes lower than ΔU, the energy barrier needed to be overcome to return to Phase I). In addition to these energy considerations, we analyze the change of the wave shape by considering the strain in the spinodal region, which is associated with negative stiffness [Fig. 1(b)]. To characterize the wave shape, we measure two time widths, t_{SpL} and t_{SpR}, in which the strain is in the spinodal region [Fig. 3(b)]. We plot the time width difference $t_{SpR} - t_{SpL}$ as shown in Fig. 3(e) in which a positive value of $t_{SpR} - t_{SpL}$ indicates that the strain stays longer in the spinodal region when the unit goes back to the initial state from Phase II. The value of $t_{SpR} - t_{SpL}$ is nearly zero initially (i.e., symmetric wave shape). However, this value increases significantly, most notably right before trapping. This is indicative of rapid growth of distortion. There are two competing processes: (1) potential-energy release (and conversion to kinetic) due to the transition from Phase I to Phase II, and (2) potential-energy rebalancing from the wave packet due to its jumping over the energy barrier (and also the spinodal region). The propagation of the subsonic wave packet shows that these two competing processes are not perfectly balanced, a requirement for genuine traveling, otherwise. Rather, the energy lost in the form of leakage of radiation wave packets dominates the energy release, as is evinced by monitoring the spinodal region. As a result, the wave packet eventually gets stuck in Phase II, nucleating a new stable phase due to the metastability of the energy landscape (cf. Refs. [21,22]). The resulting stationary patterns act effectively as impurities with respect to wave propagation, as described in the next section.

III. SCATTERING BETWEEN HARMONIC WAVES AND IMPURITIES

Based on the impurity formation described above, we now turn our focus to the scattering of a harmonic wave by such impurities in the system. We analyze the propagation of linear waves by considering the following linearized equation of motion posed on an infinite lattice:

$$m\ddot{u}_n = K_{n-1}u_{n-1} + K_n u_{n+1} - (K_{n-1} + K_n)u_n, \quad (3)$$

where K_n is K_{II} (K_I) for impurities (rest of the particles). We can thus determine the normal modes of the system by introducing the harmonic wave ansatz $u_n = e^{i(kn-\omega t)}$ where k and ω are the wave number and frequency, respectively (with $i = \sqrt{-1}$). Without impurities, we can obtain the customary dispersion relation:

$$\omega = 2\pi f = \sqrt{\frac{2K_I}{m}[1 - \cos(k)]}. \quad (4)$$

We systematically study scattering of harmonic waves by introducing a single impurity (i.e., only a single spring element is in Phase II; cf. a case of a monatomic chain with a mass defect [23]) or double impurity (two adjacent elements in Phase II) into a host chain in which all elements are initially in Phase I. Figures 4(a) and 4(b) show schematic illustrations for a chain with a single impurity ($K_{n=0} = K_{II}$) and a double impurity ($K_{n=0} = K_{n=1} = K_{II}$).

A. Theoretical analysis

To examine the effect of impurities on the scattering problem, we employ the following ansatz:

$$u_n = \begin{cases} e^{i(kn-\omega t)} + Re^{-i(kn+\omega t)} & \text{if} \quad n \leqslant 0 \\ Te^{i(kn-\omega t)} & \text{if} \quad n > 0, \end{cases} \quad (5)$$

composed of incident [denoted by I in Fig. 4(a)], reflected (R), and transmitted waves (T). This way, $|R|^2$ and $|T|^2$ are the reflection and transmission coefficients, respectively. It is important to remind the reader that, given the energy-conserving nature of the system, the incoming and outgoing wave number in free space will be the same in the case of both scattering from one and in that of scattering from more impurities. By following the same procedure used for the granular chain with Hertzian interactions [16], we plug Eq. (5) into Eq. (3), and obtain the linear system of equations

$$\mathbf{Ax} = \mathbf{b}, \quad (6)$$

with

$$\mathbf{A} = \begin{bmatrix} \gamma e^{ik} & \frac{\omega^2 m}{K_I} + e^{ik} - 1 - \gamma \\ (1+\gamma)e^{ik} - e^{2ik} - \frac{\omega^2 m}{K_I}e^{ik} & -\gamma \end{bmatrix}, \quad (7a)$$

$$\mathbf{x} = [T, \quad R]^T, \quad (7b)$$

$$\mathbf{b} = \left[-\frac{\omega^2 m}{K_I} + 1 + \gamma - e^{-ik}, \quad \gamma \right]^T, \quad (7c)$$

for the single-impurity case. Here, we define the stiffness ratio as $\gamma = K_{II}/K_I$. Solving Eq. (6) yields respectively the reflection and transmission coefficients:

$$|R|^2 = \left| \frac{(1-\gamma)(-1+e^{ik})e^{ik}}{(-1+e^{ik}) - 2\gamma e^{ik}} \right|^2, \quad (8a)$$

$$|T|^2 = \left| \frac{\gamma(1+e^{ik})}{(1-e^{ik}) + 2\gamma e^{ik}} \right|^2. \quad (8b)$$

For a chain with a double impurity, we use the following ansatz instead:

$$u_n = \begin{cases} e^{i(kn-\omega t)} + Re^{-i(kn+\omega t)} & \text{if} \quad n < 0 \\ T_1 e^{i(k_2 n-\omega t)} + R_1 e^{-i(k_2 n+\omega t)} & \text{if} \quad n = 0, 1 \\ Te^{i(kn-\omega t)} & \text{if} \quad n > 1, \end{cases} \quad (9)$$

Here, $|R_1|^2$ and $|T_1|^2$ correspond to the reflection and transmission coefficients inside the double-impurity region [see
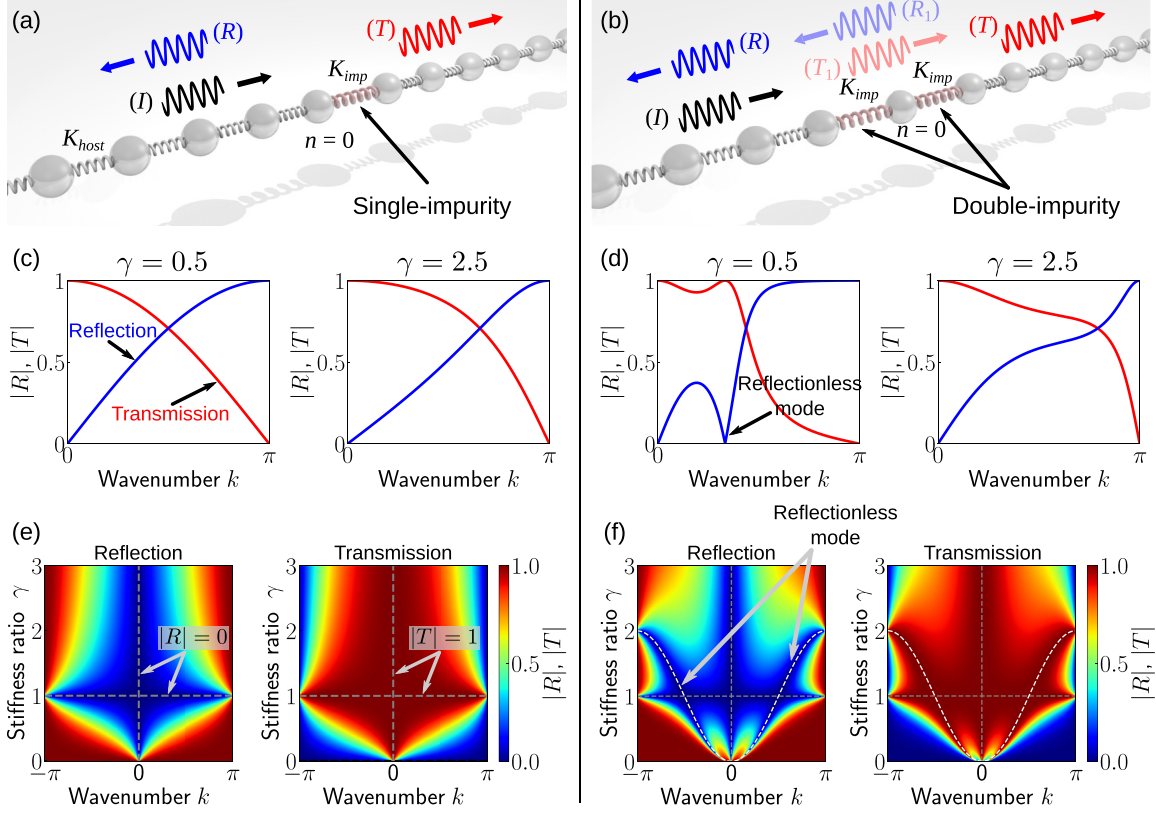
FIG. 4. Schematic illustrations for a chain with a (a) single and (b) double impurity. Analytical transmission and reflection coefficients for (c) single- and (d) double-impurity cases. The two different stiffness ratio cases (left) $\gamma = 0.5$ and (right) $\gamma = 2.5$ are shown. The reflection and transmission coefficients for (e) single- and (f) double-impurity cases are plotted as a function of stiffness ratio γ and wave number k. (e), (f) The gray dashed lines indicate $|R| = 0$ (or $|T| = 1$), and the reflectionless mode, which is expressed by Eq. (12), is denoted by the white dashed lines.

Fig. 4(b)]. Also, we define the wave number in such a region as $k_2 = k + \delta$, where δ is a difference between the wave numbers in the host chain and the impurity region. Then, following the same procedure as above, we arrive at

$$\mathbf{A} = \begin{bmatrix} 0 & e^{2ik} - \left(1 + \gamma - \frac{\omega^2 m}{K_I}\right)e^{ik} & \gamma & \gamma \\ 0 & \gamma e^{ik} & \gamma e^{i\delta}e^{ik} - 2\gamma + \frac{\omega^2 m}{K_I} & \gamma e^{-i\delta}e^{-ik} - 2\gamma + \frac{\omega^2 m}{K_I} \\ e^{2ik} & 0 & \gamma - \left(\gamma + 1 - \frac{\omega^2 m}{K_I}\right)e^{i\delta}e^{ik} & \gamma - \left(\gamma + 1 - \frac{\omega^2 m}{K_I}\right)e^{-i\delta}e^{-ik} \\ \left(\frac{\omega^2 m}{K_I} - 2\right)e^{2ik} + e^{3ik} & 0 & e^{i\delta}e^{ik} & e^{-i\delta}e^{-ik} \end{bmatrix}, \tag{10a}$$

$$\mathbf{x} = [T, \quad R, \quad T_1, \quad R_1]^T, \tag{10b}$$

$$\mathbf{b} = \left[\left(-\frac{\omega^2 m}{K_I} + 1 + \gamma\right)e^{-ik} - e^{-2ik}, \quad -\gamma e^{-ik}, \quad 0, \quad 0\right]^T, \tag{10c}$$

$$\gamma = \frac{K_{II}}{K_I}. \tag{10d}$$

In this way, we have

$$|R|^2 = \left| \frac{(1 - \gamma)(-1 + e^{ik})\{(-1 + e^{ik})^2 + 2\gamma e^{ik}\}}{-e^{ik} + (3 - 4\gamma)e^{2ik} - 3(1 - \gamma)^2 e^{3ik} + (1 - \gamma)^2 e^{4ik}} \right|^2, \tag{11a}$$

$$|T|^2 = \left| \frac{\gamma^2(1 + e^{ik})}{(-1 + e^{ik})^3 - 2\gamma(2 - 3e^{ik} + e^{2ik})e^{ik} + \gamma^2(-3 + e^{ik})e^{2ik}} \right|^2. \tag{11b}$$

For a single-impurity chain, Fig. 4(c) depicts the reflection (blue) and transmission (red) efficiency for $\gamma = 0.5$ (left panel) and $\gamma = 2.5$ (right panel), as a function of the wave number k. Both stiffness-ratio cases show a similar monotonic
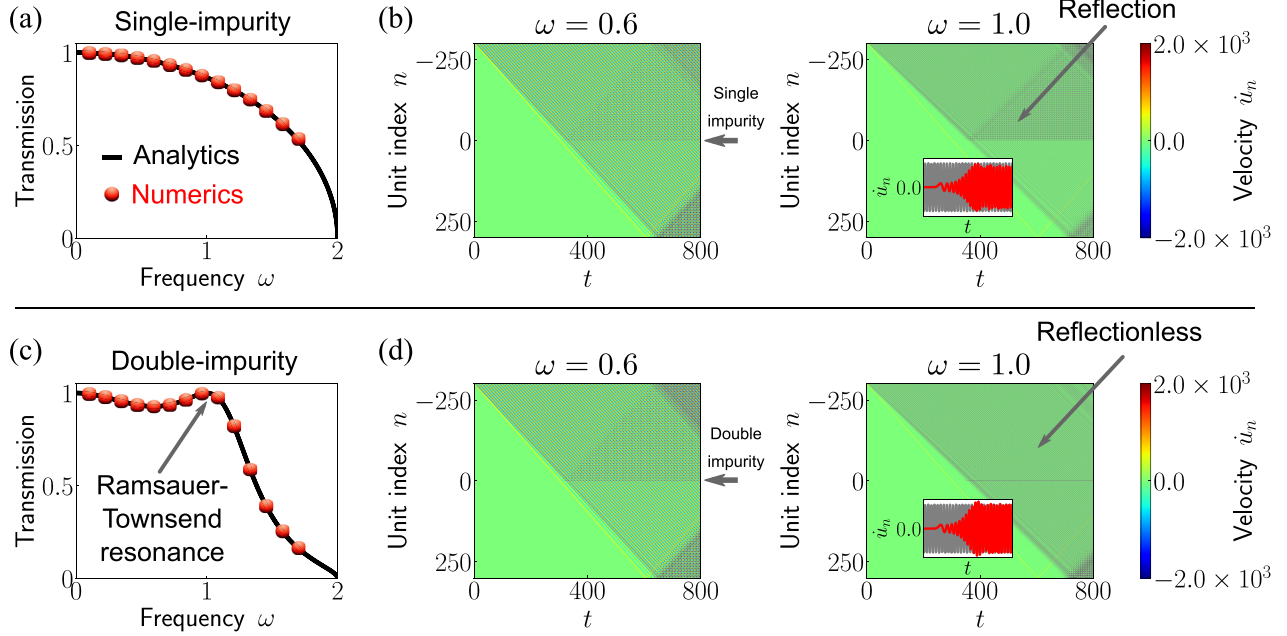
FIG. 5. Analysis of transmission. (a) Comparison between analytics (black line) and numerics (red markers) for a stiffness ratio of $\gamma = 0.5$. (b) Spatiotemporal plots of velocity profiles for excitation frequencies of (left) $\omega = 0.6$ and (right) $\omega = 1.0$, respectively. The inset shows the temporal dependence of the velocity v_n for (gray) $n = -269$ and (red) $n = 31$. (c), (d) Same as the top panels but for the case corresponding to a double-impurity chain.

increase (decrease) of the reflection (transmission). On the other hand, the double-impurity case with $\gamma = 0.5$ exhibits a nonmonotonic change of reflection and transmission. In particular, we find that there exists a reflectionless mode (i.e., the reflection coefficient is identically equal to zero) at a nonzero wave number, and complete transmission takes place at that wave number, in a way reminiscent of the Ramsauer-Townsend effect. However, if we increase the stiffness value from $\gamma = 0.5$ to 2.5, these features disappear. This reflectionless mode can be identified by setting $|R|^2 = 0$ in Eq. (11a), thus yielding:

$$\cos k = 1 - \gamma. \tag{12}$$

To thoroughly analyze the change of reflection and transmission coefficients, we plot the latter two as functions of the stiffness ratio γ and wave number k. These are shown in Figs. 4(e)–4(f) for single- and double-impurity chains, respectively. In these figures, the dashed lines indicate regions with $|R| = 0$ or $|T| = 1$. In particular, the dashed lines for the reflectionless mode are obtained from Eq. (12). The single-impurity chains show monotonic changes of reflection and transmission for any stiffness ratios as we increase or decrease the wave number from $k = 0$. As far as the double-impurity chains are concerned, our analysis shows an additional minimum reflection valley and transmission peak at nonzero wave numbers if $\gamma \leqslant 2$.

B. Numerical simulations

We now verify the above theoretical considerations by solving Eq. (2) directly. To draw comparisons between the theoretical analysis and numerical simulations we measure

the transmission coefficient numerically by analyzing velocity profiles of incident and transmitted waves under harmonic excitation [16]. For our numerical computations, we consider $N = 601$ particles ($n \in [-300, 300]$) and embed an effective impurity. The latter is in the form of a compactly supported nodes at the center of the chain corresponding to $n = 0$ for a single impurity, and $n = 0, 1$ for a double impurity. We apply harmonic excitation to the left end of the chain ($n = -300$) in the form of a force input $F_{ex} = F_0 \sin(\omega t)$ with $F_0 = 10^{-3}$ N. We then calculate the transmission coefficient from numerical simulations and analyze the velocity profile of the $n = -269$ particle for incident waves and that of the $n = 31$ particle for transmitted waves (see Appendix C for details about the calculation of the transmission from direct numerical simulations).

In Fig. 5, we compare theoretical results with numerical simulations for the stiffness ratio $\gamma = 0.5$. Figure 5(a) shows the transmission coefficients from numerical simulations (red markers) for the single-impurity case, which demonstrates excellent agreement with the analytical prediction of Eq. (8b) (solid black line). For a single-impurity chain, the reflection coefficient increases with frequency (i.e., wave number). In particular, we observe reflected waves with larger amplitude for a value of the excitation frequency of $\omega = 1.0$, compared with the case with $\omega = 0.6$, as shown in Fig. 5(b). In the case of a double-impurity chain, numerical computations capture a transmission peak at nonzero excitation frequency of about $\omega = 1.0$, denoted by the gray arrow in Fig. 5(c). In addition, we observe reflected waves for the $\omega = 0.6$ case [see left panel of Fig. 5(d)], however, such reflected waves are unnoticeable if $\omega = 1.0$ is applied to a double-impurity chain [see right panel of Fig. 5(d)], which corresponds to the reflectionless mode of the RT resonance.
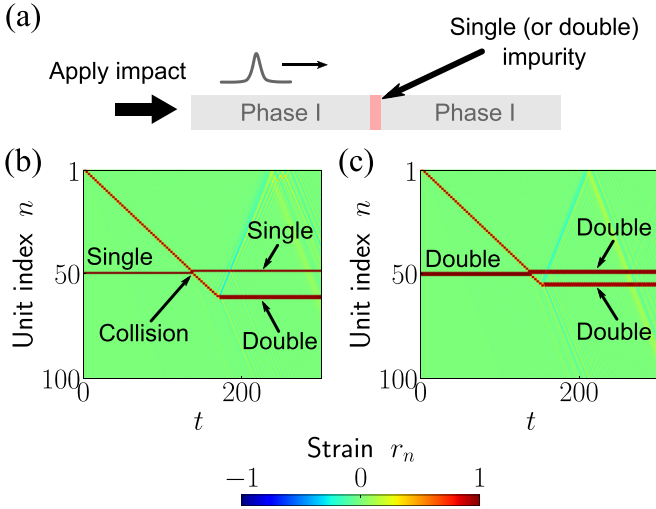
FIG. 6. (a) Schematic illustration of a collision of a propagating wave packet with an impurity. (b), (c) Spatiotemporal plots of strain wave profiles for the (b) single- and (c) double-impurity cases. We apply the initial velocity [$v_1(t = 0) = 0.55$] to the first particle to generate the subsonic propagating wave packet.

IV. CHAIN WITH MULTIPLE IMPURITIES

With a firm understanding of scattering by single and double effective impurities, we consider now the formation of multiple impurities in the chain and demonstrate an interesting application of the reflectionless mode, specifically for reconfigurable manipulation of linear wave propagation. In Sec. II, we observed the formation of a (double) impurity due to the trapped energy transported by a propagating wave packet. In this section, we show that the collision of such a wave packet with an impurity can introduce additional impurities.

To demonstrate this, we perform numerical simulations by generating a propagating wave packet in a chain with a single or double impurity under impact [see Fig. 6(a)]. The stiffness parameters used in this section are $K_I = 1$ and $K_{II} = 1.5$ with an initial velocity of $v_1 = 0.55$ applied to the first particle. This generates a wave packet as shown in Fig. 6(b) which corresponds to the single-impurity case. We find that a wave packet penetrates through a single-impurity but its propagation is stopped before reaching the end of the chain, leading to an additional double impurity besides the initial single impurity. Note that the initial impurity is shifted backward by one spatial node. If a wave packet collides with a double impurity, then an additional double impurity is formed once the solitary wave passes through the impurity region [Fig. 6(c)].

We examine such interactions between a subsonic wave packet and an impurity by considering the energy change before and after the collisions. Figure 7(a) shows the spatiotemporal plot of the total energy E_n for the single-impurity case [corresponding to Fig. 6(a)], and we also track the peak energy of the subsonic wave packet as shown in Fig. 7(b). After the collision, some of the energy is reflected [see also the energy decrease of the transmitted wave packet as shown in Fig. 7(b)]. However, this reflected energy is not sufficient to generate another propagating wave packet, and it partly gets trapped causing the backward shift of the impurity, which
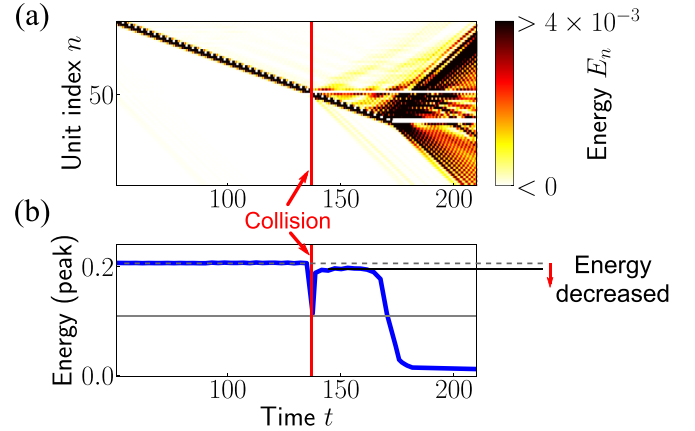
FIG. 7. Collision of a (subsonic) propagating wave packet with a single impurity. (a) Surface plot of the energy $E_n(t) = \frac{1}{2}m\dot{u}_n^2(t) + U_n(t)$ where U_n is the bistable potential-energy function as shown in Fig. 1(c). The red vertical line indicates the collision point. (b) The peak energy of the propagating wave packet is shown as a function of time.

is followed by the trapping of the transmitted wave packet. Therefore, our numerical results demonstrate the feasibility of creating multiple impurities via collisions of the propagating wave packet with impurities, instead of directly manipulating the phase of the individual units.

Having confirmed the formation of multiple impurities in our system, a natural question to ask is whether the reflectionless mode can be observed in a chain with multiple impurities [see Fig. 8(a) for a schematic]. Figure 8(b) shows the analytical reflection and transmission coefficients for a chain with multiple double impurities ($\gamma = 1.5$) where we identify the reflectionless mode at $\omega = 1.73$. To examine the scattering between harmonic waves and multiple impurities, we consider a chain in which four double impurities are embedded. Then, we apply two different harmonic excitation inputs to the chain for comparison: $\omega_{ex} = 1.10$ and 1.73. Here, the amplitude of excitation force is $F_0 = 0.14$. Figure 8(c) shows the space-time contour plot of strain wave propagation for an excitation frequency of $\omega_{ex} = 1.10$. As predicted, we observe the reflected waves. Once these waves reach the left end of the chain, the amplitude of the strain becomes large enough to trigger a phase transition toward Phase II propagating in the chain due to the amplitude-dependent nature of our bistable system. On the other hand, if $\omega_{ex} = 1.73$, the wave passes through the impurity region without noticeable reflected waves and no particle overcomes the energy barrier necessary for a phase transition. Once again, our detailed understanding of the scattering problem enables a characterization of the associated reflectionless dynamics within the chain.

V. CONCLUSIONS AND FUTURE DIRECTIONS

In the present work, we investigated the formation of effective impurities in a bistable chain arising from the trapping of propagating wave packets formed upon impact. We numerically studied the amplitude dependence of the impact speed on the behavior of linear and nonlinear wave propagation in the bistable chain whose spring elements exhibit an asymmetric
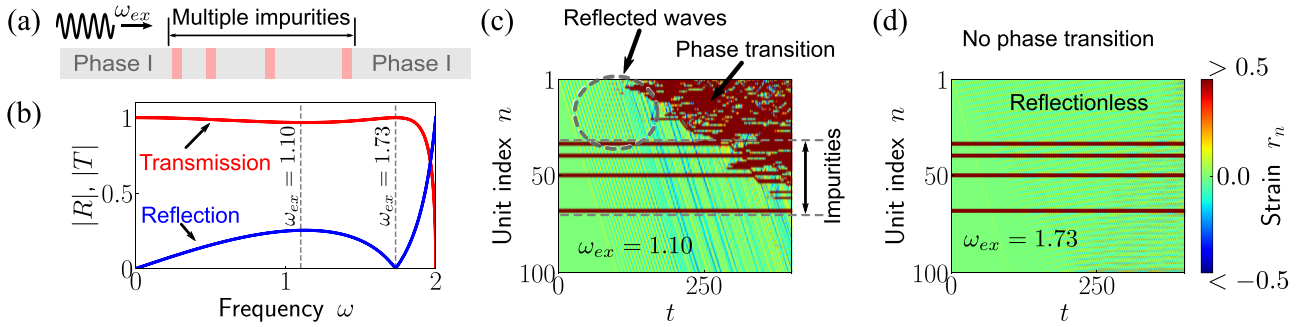
FIG. 8. Scattering by multiple double impurities. (a) The schematic illustration highlights the application of a harmonic excitation (with excitation frequency ω_{ex}) to the first unit ($n = 1$) of the chain with multiple double impurities. The stiffness parameters for the host and impurities are $K_{\text{host}} = 1$ and $K_{\text{imp}} = 1.5$, respectively. (b) The transmission and reflection coefficients for the double impurity with $\gamma = 1.5$ are shown as a function of frequency ω. Surface plots of strain wave propagation are presented for (c) $\omega_{ex} = 1.10$ and (d) $\omega_{ex} = 1.73$.

energy landscape. In particular, we used numerical simulations to investigate the propagation of wave packets formed upon impact. Interestingly, our numerical analysis results revealed that, due to the formation of an oscillatory tail during time propagation, the resulting moving wave packet loses its energy and eventually gets trapped into a lower-energy stationary state.

Based on this emergent localization, we systematically studied the interaction of impurities with linear waves and moving wave packets. For the linear wave case, we examined the scattering between harmonic waves and localized structures. In the system with a single impurity, our analytical and numerical results showed that the transmission coefficient monotonically decreases as the harmonic input excitation increases. On the other hand, the bistable chain with two adjacent units in the lower energy phase exhibits a reflectionless mode due to the analog of the well-known Ramsauer-Townsend effect.

Additionally, we explored the interaction between a single or double impurity and a propagating wave packet. The latter can pass through the impurity instead of being reflected or merged into the existing impurity, however, the wave packet eventually gets trapped in a low-energy state, which creates an additional impurity in the chain. Based on this feasibility of adding multiple impurities, together with the reflectionless mode, we further demonstrated that a phase-transition front, or a reflectionless propagation can be "engineered" in the chain with multiple double impurities, depending on the input harmonic frequency. Given that the impurities created by moving wave packets in a bistable chain can change the linear and nonlinear wave dynamics, such bistable systems can be useful for controlling a reconfigurable structure in a flexible manner. It should be noted in passing that such impurities can be removed from the system by generating the propagation of phase transition fronts [12] (see also Appendix D for numerical demonstrations). This, in principle, allows reprogramming of the system's linear dynamic response.

This work paves the path for future efforts. From the theoretical perspective, the analytical derivation of exact traveling solutions in the present setup would be an interesting problem to pursue by using techniques such as those discussed in Refs. [24,25] for a diatomic lattice (see also Ref. [20]). On

the other hand, a systematic existence and stability analysis of traveling waves will be of particular relevance to the present setting. To that end, spectral collocation techniques such as those presented in Ref. [26] could be employed. An especially important aspect of such considerations concerns the nature of the propagating subsonic wave packets. While these spontaneously emerge as a result of the initial impact, they also shed energy away only to eventually (and spontaneously) transform themselves to compactly supported standing excitations. A further understanding of potential traveling solutions associated with these wave packets and of the energetics of the above process would be especially useful for the further unveiling of the dynamics of such bistable lattices. For example, precise prediction and control of trapping behavior would be useful for altering the dynamic properties of multistable (engineering) systems, such as deployable space structures and reconfigurable mechanical signal processing units, locally and/or globally. Of course, here we have only considered a piecewise linear problem, while realistic systems could be smooth nonlinear variants thereof. Also, the physical realization of such platforms generally involves both on-site and intersite dissipative effects, which leads to questions of how damping affects the strong interaction between linear waves and the propagating wave packets arising from the subsonic nature, and of whether the formation of an oscillatory tail can be accelerated (or decelerated). It will also be especially interesting to explore which of the ramifications of the present setting (including potential subsonic traveling patterns, compactly supported standing waves, and their respective stability traits and scattering implications) are particular to the present setting and which generalize, including, potentially, in higher-dimensional settings. These directions are currently under consideration and their studies will be reported in future presentations.
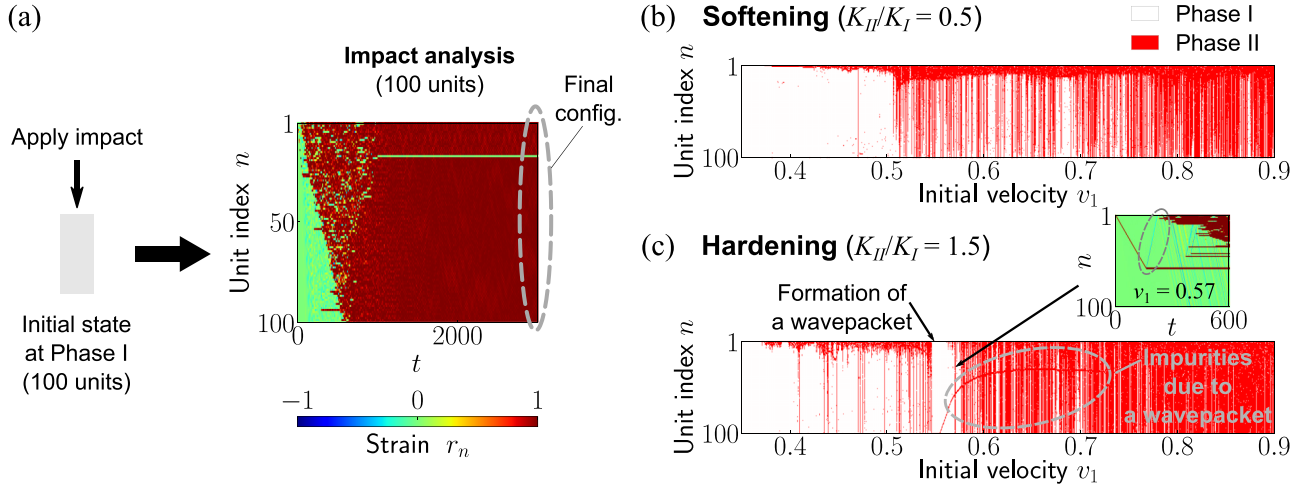
FIG. 9. Amplitude-dependent phase-transition behavior. (a) Schematic illustration for examining the steady-state configuration after an impact is applied to the chain. We extract the final configurations of the chain at $t = 3000$ and present them as a function of the impact velocity v_1 for (b) the softening ($K_{II}/K_I = 0.5$) and (c) hardening ($K_{II}/K_I = 1.5$) chains.

APPENDIX A: AMPLITUDE-DEPENDENT PHASE TRANSITION

To investigate the impact-amplitude-dependent phase transition, we conduct numerical simulations on a chain with 100 particles by applying impacts of varying amplitude, as shown in Fig. 9(a). All of the spring elements are initially in Phase I, and an initial impact is applied to the first particle. Numerical simulations are performed for $t \in [0, 3000]$ to allow sufficient time to achieve a steady-state configuration. We demonstrate the final configuration at $t = 3000$, representing the steady-state configuration after impact, as a function of the amplitude of impact velocity. The corresponding numerical simulation results for the softening case ($K_{II}/K_I = 0.5$) are shown in Fig. 9(b), whereas those for the hardening case ($K_{II}/K_I = 1.5$) are shown in Fig. 9(c). The other numerical constants are (K_S, r_S, r_{II}) = ($-1, 0.4, 1$). In the figures, the white and red colors indicate the final states in Phase I and Phase II, respectively. For the softening case, the phase transition tends to be localized around the left end of the chain for smaller-amplitude impacts, and as we increase the amplitude of the impact input, the phase-transition wave propagates in the chain and most of the spring elements move to Phase II states.

For the hardening chain, we obtain more interesting behavior, specifically the formation of a propagating wave packet. In Fig. 9(c), we find that phase transition occurs only near the left end of the chain for smaller amplitude impact, which is similar to the softening case. However, and in the specific amplitude regime (denoted by the black arrow in the figure), no particle is in Phase II in the final configuration due to the formation of a (subsonic) wave packet propagating from one end to the other one of the chains. If we increase the impact amplitude from that regime, a (subsonic) wave packet stops propagating

in the middle of the chain, which forms an impurity, as we discussed in Sec. II. Note that when the propagation of a wave packet is brought to halt, waves propagating toward the left end of the chain are generated [see the red dashed circle in the inset of Fig. 9(c)], which sometimes induces phase-transition behavior.

APPENDIX B: PADÉ APPROXIMATION OF A SUPERSONIC SOLITARY WAVE

To examine a supersonic solitary wave shown in Fig. 2(d), we use the Padé approximation which has been previously employed to study solitary waves in a (nonintegrable) bistable chain [13,14]. First, we derive the advance-delay differential equation in terms of the strain variable r_n:

$$m\ddot{r}_n = F(r_{n-1}) + F(r_{n+1}) - 2F(r_n), \qquad (B1)$$

where F is force as a function of strain [see Eq. (1)]. By introducing the ansatz $r_n(t) = r(n - V_{tw}t) = r(\zeta)$, we rewrite Eq. (B1) as follows:

$$V_{tw}^2 r = \Lambda(D)F(r), \qquad (B2)$$

where

$$\Lambda(D) = \frac{1}{D^2}\left[4\sinh^2\left(\frac{D}{2}\right)\right], \qquad (B3)$$

and D is the differential operator with respect to ζ. Based on Refs. [13,14], we introduce the Padé approximation of order $[m, n]$ (m and n are the polynomial order of the numerator and denominator of the Padé approximation, respectively) to simplify the operator $\Lambda(D)$. If $[m, n] = [0, 2]$, the Padé approximant is expressed by

$$\Lambda(D) = \left(I - \frac{D^2}{12}\right)^{-1}, \qquad (B4)$$

where I is the identity operator.

Next, we seek a solitary wave solution by considering the three distinctive regions; Phase I ($r < r_a$), Spinodal region ($r_a < r < r_b$), and Phase II ($r > r_b$) as shown in Fig. 1(b).
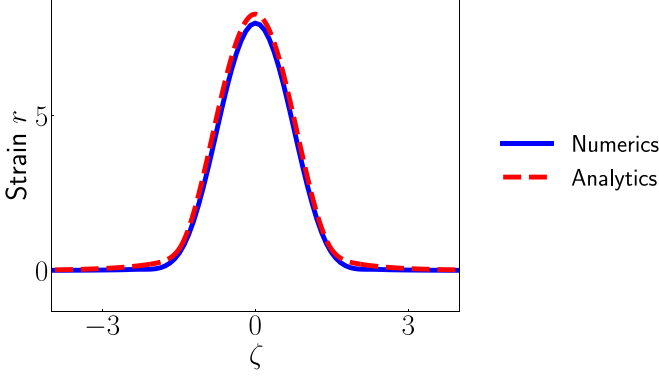
FIG. 10. Wave form analysis of the supersonic solitary wave. The blue solid line indicates the strain profile of the supersonic solitary wave with the wave speed of 1.076 obtained from the simulation [see Fig. 2(d)]. The red dashed line indicates the analytical solution based on the Padé approximation [Eq. (B5)].

Let r_I, r_S, and r_{II} be the solitary wave solutions in Phase I, Spinodal, and Phase II regimes; we obtain the following solutions by using Eqs. (B2) and (B4):

$$r_I(\zeta) = r_a e^{-\lambda_1(\zeta - \zeta_a)}, \tag{B5a}$$

$$r_S(\zeta) = \frac{r_b - p_2}{\cos(\lambda_2 \zeta_b)} \cos(\lambda_2 \zeta) + p_2, \tag{B5b}$$

$$r_{II}(\zeta) = (r_a - p_S) \cosh[\lambda_S(\zeta - \zeta_a)]$$
$$- \frac{\lambda_1}{\lambda_S} r_a \sinh[\lambda_S(\zeta - \zeta_a] + p_S, \tag{B5c}$$

where

$$p_{II} = \frac{(K_S - 1)r_a + (K_{II} - K_S)r_b}{K_{II} - V_{tw}^2}, \tag{B6}$$

$$p_S = \frac{(1 - K_S)r_a}{V_{tw}^2 - K_S}, \tag{B7}$$

$$\lambda_I^2 = 12\left(1 - \frac{1}{V_{tw}^2}\right), \tag{B8}$$

$$\lambda_{II}^2 = 12\left(\frac{K_{II}}{V_{tw}^2} - 1\right), \tag{B9}$$

$$\lambda_S^2 = 12\left(1 - \frac{K_S}{V_{tw}^2}\right). \tag{B10}$$

Also,

$$\zeta_b = \frac{1}{\lambda_{II}}\left[\pi - \tan^{-1}\left(\frac{\lambda_S\sqrt{(r_b - p_S)^2 - (r_a - p_S)^2 + r_a^2\lambda_I^2/\lambda_S^2}}{\lambda_{II}(p_{II} - r_b)}\right)\right], \tag{B11a}$$

$$\zeta_a = \zeta_b - \frac{2}{\lambda_S}\tanh^{-1}\left[\frac{\lambda_S(r_a - r_b)}{\lambda_I r_a + \lambda_{II}(r_b - p_{II})\tan(\lambda_{II}\zeta_b)}\right]. \tag{B11b}$$

In Fig. 10, we compare the solitary wave solution based on the Padé approximation (red dashed line) with the
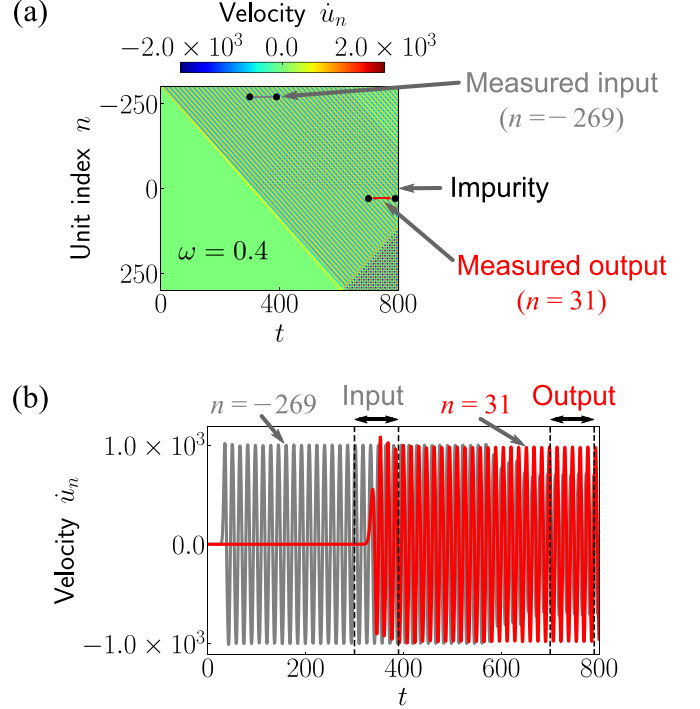
FIG. 11. Numerical simulations to obtain the transmission coefficient. (a) Spatiotemporal plot of velocity. We embed a single impurity (stiffness ratio $\gamma = 0.5$) in a chain composed of 601 units and apply a harmonic excitation ($\omega = 0.4$) to the chain. (b) Temporal distribution of the velocity profiles v_n for (gray) $n = -269$ and (red) $n = 31$.

strain profile of the (supersonic) solitary wave with $V_{tw} = 1.076$ from the simulation [see Fig. 2(d)] (blue solid line). The numerical parameters used in this analysis are the same as those of Sec. II. The analytical solution based on the Padé approximation agrees well with the numerical simulation.

APPENDIX C: TRANSMISSION FOR VARIOUS STIFFNESS RATIOS

Figure 11(a) shows a spatiotemporal plot of particle velocities for the case corresponding to $\omega = 0.4$. To calculate the transmission coefficient from numerical simulations, we analyze the velocity profile of the $n = -269$ particle for incident waves and that of the $n = 31$ particle for transmitted waves. In Fig. 11(b), we present the temporal distribution of the velocity profiles v_n for the above-mentioned values of n where we calculate the average amplitudes from the steady-state region bounded by the vertical dashed lines. Let A_I and A_T be the average amplitudes of the incident waves measured at $n = -269$ and transmitted waves at $n = 31$. Then, we calculate numerically the transmission as $T_{sim} = A_T/A_I$.

Besides the case with stiffness ratio $\gamma = 0.5$ discussed in Sec. III, we additionally conduct numerical simulations for $\gamma = 1.5$ and 2.5. In Fig. 12, we show numerical results for a chain with a single-impurity [Figs. 12(a) and 12(b)], and a double-impurity [Figs. 12(c) and 12(d)]. The left (right) two
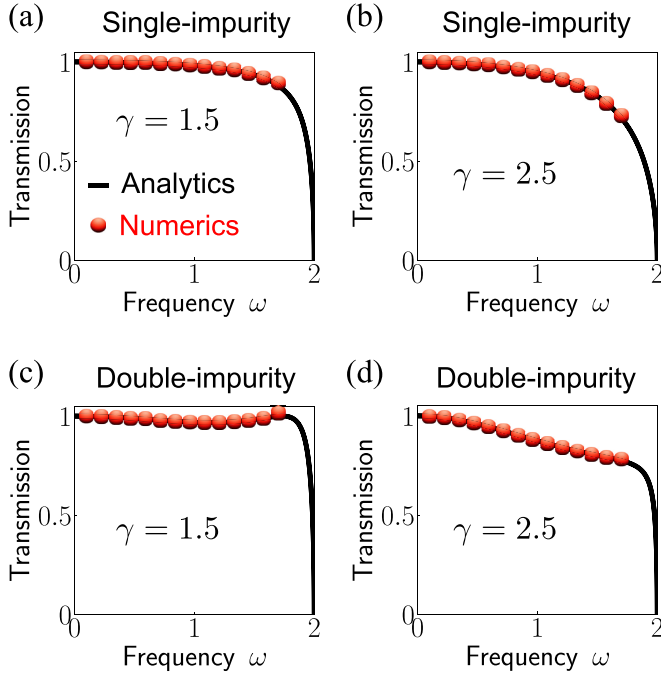
FIG. 12. Analytical transmission compared with numerical simulations for (a), (b) single-impurity and (c), (d) double-impurity cases. We calculate transmission coefficients for stiffness ratios (left) $\gamma = 1.5$ and (right) $\gamma = 2.5$.

plots are obtained for a stiffness ratio of $\gamma = 1.5$ ($\gamma = 2.5$). Similarly to the comparison for $\gamma = 0.5$ in the main text, we confirm excellent agreement between numerical simulation results and analytical transmission coefficients for all four cases.

APPENDIX D: IMPURITY DISAPPEARANCE VIA PROPAGATION OF PHASE BOUNDARY

To further reveal the nature of a bistable lattice, we present in this section a way to bring a chain with pre-existing effective impurities to a homogeneous configuration by utilizing the propagation of phase boundaries. To achieve this, we control the displacement of the first particle at constant speed v_1. The numerical parameters used in our analysis are the same as those of Sec. IV. Figure 13(a) shows the strain profiles for a homogeneous chain in which all spring elements are initially in Phase I. We apply a constant velocity of $v_1 = 1.2$ to the first particle in order to control its displacement. As one can observe in other bistable lattices (e.g., Refs. [27–29]), phase transitions from Phase I to Phase II take place and the phase boundary separating the phases (denoted by the gray dashed line) moves at constant speed in the chain. Note that the linear (sonic) waves propagate faster than the phase boundary (see the black dashed line). By embedding multiple double impurities in a host homogeneous chain, we perform the same analysis. In Fig. 13(b), our numerical results show the propagation of phase boundaries in a manner similar to the homogeneous case. These phase transitions bring all spring elements to Phase II. In this way, the bistable chain can achieve a homogeneous configuration (Phase II) without impurities. Although the overall strain profiles for the multiple impurities case is similar to that for the homogeneous case, the propagating phase boundaries experience phase shifts at the locations of the impurities.

To quantify this phase-shifting behavior we calculate the speed of the phase boundary propagating in the system by fitting a straight line to the phase boundary [see the gray dashed line in Fig. 13(b)]. In Fig. 13(c) the phase boundary speed V_{PB} is presented as a function of the applied velocity for displacement control v_1. The gray and red markers indicate the phase boundary speed for a homogeneous chain and a chain with multiple impurities, respectively. The solid black line is the analytical phase boundary speed for a homogeneous chain [30–32]. If the applied velocity is small, we find that the phase boundary speed v_{PB} (obtained from a chain with impurities) is higher than that of the homogeneous case because the linear waves propagate faster in Phase II (impurity locations) due to $K_{II} > K_I$. The inset in Fig. 13(c) shows the difference between the homogeneous and
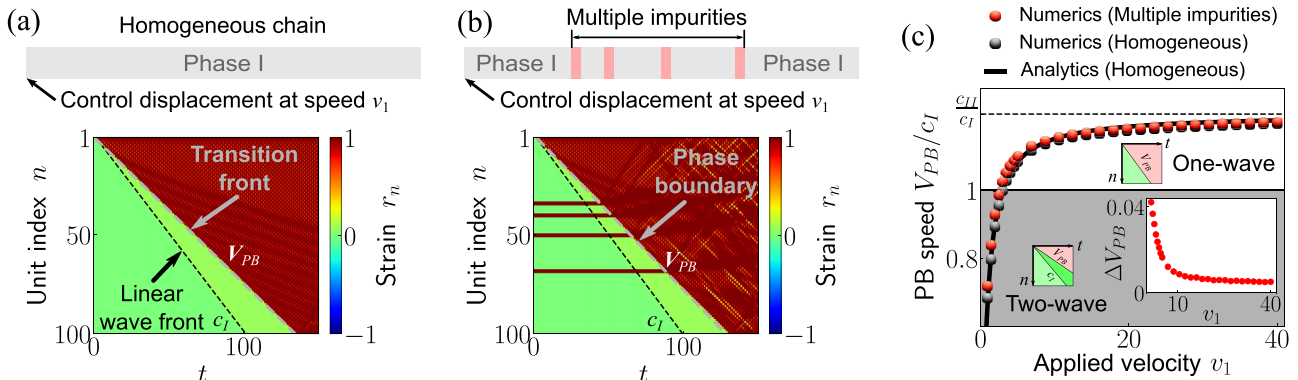
FIG. 13. Effect of multiple double impurities on phase transitions. Spatiotemporal plots for (a) a homogeneous chain (Phase I) and (b) a chain with double impurities ($K_{\mathrm{imp}} = K_{II} = 1.5$). We control the displacement of the first unit at constant speed $v_1 = 1.2$. The gray (black) dashed lines indicate the phase boundary (linear wavefront). (c) We plot the speed of the phase boundary (V_{PB}) as a function of the applied speed v_1. The inset shows the difference between the phase boundary speeds for the homogeneous chain without impurities and the chain with multiple impurities, which is defined as $\Delta V_{PB} = V_{PB}^i - V_{PB}^h$.
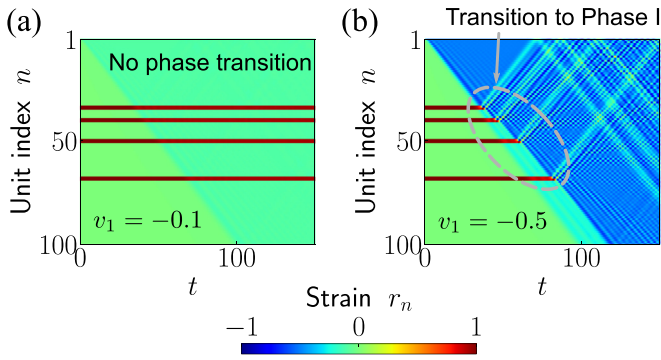
FIG. 14. A chain with multiple impurities under tension. To apply the tension, we control the displacement of the first particle at constant speed v_1. Spatiotemporal plots of the strain wave profiles for (a) $v_1 = -0.1$ and (b) $v_1 = -0.5$.

multiple impurities cases, defined as $\Delta V_{PB} = (V_{PB}^i - V_{PB}^h)/c_I$, where V_{PB}^h and V_{PB}^i are the phase boundary speeds calculated

from the homogeneous and multiple-impurity cases, respectively. As already mentioned above, the gap between these two cases is larger for smaller applied velocity and smaller for larger applied velocity, which means that the propagation of the phase boundary is insensitive to multiple impurities in a chain. This is due to the fact that the phase boundary speed at high impact velocities approaches the sonic wave speed.

If we control the displacement of the first particle in the opposite direction it is also possible to bring all spring elements to Phase I. Figures 14(a) and 14(b) show the numerical simulation results for two different applied velocities: $v_1 = -0.1$ and $v_1 = -0.5$, respectively. Interestingly, if the applied velocity is not sufficiently large, the embedded impurities remain in Phase II as shown in Fig. 14(a). However, if $v_1 = -0.5$, the large-amplitude waves are generated and the impurities are brought back to Phase I. Here, we also observe that the waves experience phase shifts due to impurities.

[1] S. Shan, S. H. Kang, J. R. Raney, P. Wang, L. Fang, F. Candido, J. A. Lewis, and K. Bertoldi, Adv. Mater. **27**, 4296 (2015).

[2] A. Rafsanjani, A. Akbarzadeh, and D. Pasini, Adv. Mater. **27**, 5931 (2015).

[3] K. Bertoldi, V. Vitelli, J. Christensen, and M. Van Hecke, Nat. Rev. Mater. **2**, 17066 (2017).

[4] E. Hawkes, B. An, N. M. Benbernou, H. Tanaka, S. Kim, E. D. Demaine, D. Rus, and R. J. Wood, Proc. Natl. Acad. Sci. USA **107**, 12441 (2010).

[5] T. Chen, O. R. Bilal, K. Shea, and C. Daraio, Proc. Natl. Acad. Sci. USA **115**, 5698 (2018).

[6] K. A. Seffen and S. Pellegrino, Proc. R. Soc. London, Ser. A **455**, 1003 (1999).

[7] K. Kuribayashi, K. Tsuchiya, Z. You, D. Tomus, M. Umemoto, T. Ito, and M. Sasaki, Mater. Sci. Eng., A **419**, 131 (2006).

[8] N. Nadkarni, C. Daraio, and D. M. Kochmann, Phys. Rev. E **90**, 023204 (2014).

[9] N. Nadkarni, A. F. Arrieta, C. Chong, D. M. Kochmann, and C. Daraio, Phys. Rev. Lett. **116**, 244501 (2016).

[10] J. R. Raney, N. Nadkarni, C. Daraio, D. M. Kochmann, J. A. Lewis, and K. Bertoldi, Proc. Natl. Acad. Sci. USA **113**, 9722 (2016).

[11] L. Jin, R. Khajehtourian, J. Mueller, A. Rafsanjani, V. Tournat, K. Bertoldi, and D. M. Kochmann, Proc. Natl. Acad. Sci. USA **117**, 2319 (2020).

[12] H. Yasuda, L. M. Korpas, and J. R. Raney, Phys. Rev. Appl. **13**, 054067 (2020).

[13] S. Katz and S. Givli, Extreme Mech. Lett. **22**, 106 (2018).

[14] S. Katz and S. Givli, Phys. Rev. E **100**, 032209 (2019).

[15] A. Vainchtein, Phys. Rev. E **102**, 052218 (2020).

[16] A. J. Martínez, H. Yasuda, E. Kim, P. G. Kevrekidis, M. A. Porter, and J. Yang, Phys. Rev. E **93**, 052224 (2016).

[17] L. M. Brekhovskikh, *Waves in Layered Media* (Academic Press, Cambridge, 1960).

[18] J. Sakurai, *Modern Quantum Mechanics* (Addison-Wesley, Boston, 1994).

[19] G. Friesecke and R. L. Pego, Nonlinearity **12**, 1601 (1999).

[20] L. Truskinovsky and A. Vainchtein, Phys. Rev. E **90**, 042903 (2014).

[21] A. M. Balk, A. V. Cherkaev, and L. I. Slepyan, J. Mech. Phys. Solids **49**, 131 (2001).

[22] S. C. Ngan and L. Truskinovsky, J. Mech. Phys. Solids **50**, 1193 (2002).

[23] P. Deymier and K. Runge, *Duality, Coherence and Wave-Mixing: An Introduction to the Emerging New Science of Sound* (Springer, Berlin, 2017).

[24] A. Vainchtein, J. Mech. Phys. Solids **58**, 227 (2010).

[25] A. Vainchtein and P. Kevrekidis, J. Nonlinear Sci. **22**, 107 (2012).

[26] J. Eilbeck and R. Flesch, Phys. Lett. A **149**, 200 (1990).

[27] L. Slepyan, A. Cherkaev, and E. Cherkaev, J. Mech. Phys. Solids **53**, 407 (2005).

[28] L. Truskinovsky and A. Vainchtein, SIAM J. Appl. Math. **66**, 533 (2006).

[29] B. Deng, P. Wang, V. Tournat, and K. Bertoldi, J. Mech. Phys. Solids **136**, 103661 (2020).

[30] R. Abeyaratne and J. K. Knowles, *Evolution of Phase Transitions* (Cambridge University Press, Cambridge, 2006).

[31] Q. Zhao and P. K. Purohit, Modell. Simul. Mater. Sci. Eng. **22**, 045004 (2014).

[32] R. Khajehtourian and D. M. Kochmann, Extreme Mech. Lett. **37**, 100700 (2020).